Laser-induced Coulomb explosion of heteronuclear alkali-metal dimers on helium nanodroplets

Simon H. Albrechtsen [1,*] Jeppe K. Christensen,[2,*] Rico Mayro P. Tanyag [2] Henrik H. Kristensen [1] and Henrik Stapelfeldt [2,†]

[1]*Department of Physics and Astronomy, Aarhus University, Ny Munkegade 120, DK-8000 Aarhus C, Denmark*
[2]*Department of Chemistry, Aarhus University, Langelandsgade 140, DK-8000 Aarhus C, Denmark*

A sample mixture of alkali-metal homonuclear dimers, Ak_2 and Ak'_2, and heteronuclear dimers, $AkAk'$, residing on the surface of helium nanodroplets are Coulomb exploded into pairs of atomic alkali-metal cations, (Ak^+, Ak^+), (Ak'^+, Ak'^+), and (Ak^+, Ak'^+), following double ionization induced by an intense 50-fs laser pulse. The measured kinetic-energy distribution $P(E_{kin})$ of both the Ak^+ and Ak'^+ fragment ions contains overlapping peaks due to contributions from Coulomb explosion of the homonuclear and heteronuclear dimers. From $P(E_{kin})$, we determine the distribution of internuclear distances $P(R)$ via the Coulomb-explosion imaging principle. Using coincident filtering based on momentum division between the two fragment ions, we demonstrate that the individual $P(E_{kin})$ distributions pertaining to ions from either hetero- or homonuclear dimers can be retrieved. This filtering method works through the concurrent detection of two-dimensional velocity images of the Ak^+ and the Ak'^+ ions implemented through the combination of a velocity-map-imaging spectrometer and a TPX3CAM detector. The key finding is that $P(R)$ can be measured for any specific dimer in the unavoidably mixed sample of hetero- and homonuclear alkali-metal dimers. We report results for LiK and NaK, which were previously unmeasurable by the Coulomb-explosion technique. Our method should also work for other heteronuclear dimers and for differentiating between different isotopologues of any of the dimers.

I. INTRODUCTION AND BACKGROUND

Nanometer-sized droplets of liquid helium provide a unique medium for studying the structure and dynamics of atoms, molecules, and clusters [1–5]. While most of such dopants are located in the interior of the droplets, alkali-metal atoms and small clusters thereof play a special role by residing on the droplet surface [6–12]. Notably, alkali-metal dimers and trimers have been extensively investigated for more than 25 years. Experimentally, the main method used is absorption spectroscopy, in which pulsed or continuous-wave laser beams excited the dimers or trimers electronically with vibrational state resolution. Such experimental studies established that the dimers and trimers reside on the surface and, furthermore, that the dimers are mainly formed in the lowest-lying triplet state and the trimers are mainly formed in the lowest-lying quartet state [13–19].

Recently, it was demonstrated that Coulomb explosion induced by irradiation with an intense femtosecond laser pulse provides an alternative way to explore alkali-metal dimers and trimers, for instance, Na_2 and Na_3, made of a single alkali-metal species [20,21]. In the case of an alkali-metal dimer, the dimer is first doubly ionized through multiphoton absorption from an intense femtosecond laser pulse with a central wavelength typically around 800 nm. The resulting

dication Ak_2^{2+} then breaks apart into two Ak^+ fragment ions:

$$Ak_2 + N\hbar\omega \rightarrow Ak_2^{2+} + 2e^-,$$
$$Ak_2^{2+} \rightarrow Ak^+ + Ak^+ \qquad (1)$$
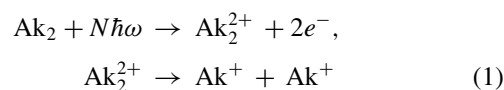
(see Fig. 1). Since the double-ionization process removes the two valence electrons, Ak_2^{2+} has a closed-shell structure and is therefore formed in only one state. As such, there is only a single, repulsive potential curve V_{dicat} for Ak_2^{2+}. For the equilibrium internuclear distances of Ak_2 in either the $1\,^1\Sigma_g^+$ or $1\,^3\Sigma_u^+$ state, V_{dicat} is, to a good approximation, given by a Coulomb potential:

$$V_{dicat} \approx V_{Coul} = \frac{14.4\,eV}{R(\text{Å})} + 2I_p(Ak) \qquad (2)$$

(see Fig. 1), where $I_p(Ak)$ is the ionization potential of Ak.

The single repulsive potential curve ensures a one-to-one correspondence between the initial internuclear distance R of the dimer and the final kinetic energy E_{kin} of each of the Ak^+ fragment ions. If the dimer is made up of two alkali-metal atoms with the same mass, for instance, $^{39}K_2$, then energy and momentum conservation leads to $E_{kin} = \frac{7.2\,eV}{R(\text{Å})}$ in the Coulomb-potential approximation. One useful consequence of the one-to-one (R, E_{kin}) correspondence is that measurement of E_{kin} makes it possible to distinguish between Ak_2 in the $1\,^1\Sigma_g^+$ and $1\,^3\Sigma_u^+$ states [20]. It was found that dimers are preferentially formed in the $1\,^3\Sigma_u^+$ state. The quantum state sensitivity was exploited to record laser-induced nonadiabatic alignment dynamics of alkali-metal homonuclear dimers in

*These authors contributed equally to this work.
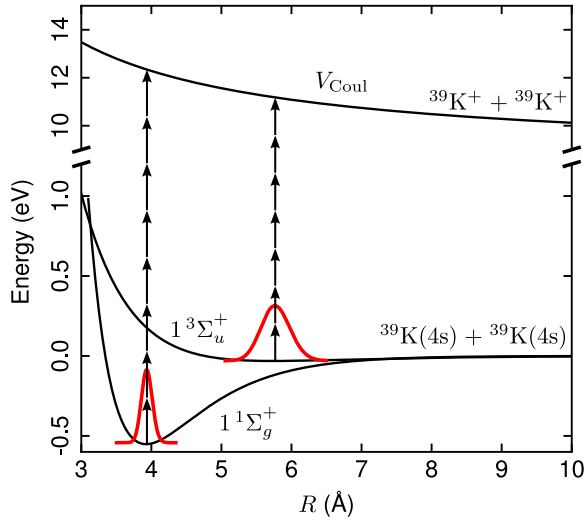†henriks@chem.au.dk

FIG. 1. Illustration of laser-induced Coulomb explosion of an alkali-metal dimer using K_2 as an example. The energy diagram depicts the potential curves for the $1\,^1\Sigma_g^+$ state [22] and the $1\,^3\Sigma_u^+$ state [23], with the square of the corresponding vibrational ground-state wave functions given in red. The potential curve for K_2^{2+} is shown as a Coulomb potential [see Eq. (2)]. The black arrows represent the photons (not to scale) of the laser pulse, illustrating the multiphoton absorption process that causes double ionization of K_2 and thereby Coulomb explosion into a pair of K^+ ions.

both the triplet and singlet states [24]. With this method the distribution of internuclear distances $P(R)$ for the dimers in the two quantum states can also be determined [21]. This approach has been extended to femtosecond time-resolved measurements of $P(R)$ for vibrating dimers [25].

In the current work, we explore Coulomb explosion of heteronuclear alkali-metal dimers, AkAk′, on the surface of helium droplets, where Ak and Ak′ are two different alkali-metal atoms, for instance, ^{7}Li and ^{39}K. At first, it may seem like a straightforward extension of the former work on homonuclear dimers, but due to the way the heteronuclear dimers are created, that is not the case. In practice, an AkAk′ dimer is formed by passing helium droplets through two serially arranged pickup cells. A droplet can then pick up an Ak atom in the first cell and an Ak′ atom in the second cell, which may lead to the formation of an AkAk′ heteronuclear dimer. The statistical nature of the pickup process implies, however, that some droplets pick up two Ak atoms or two Ak′ atoms, leading to the formation of an Ak_2 or an Ak_2' homonuclear dimer [26,27].

For the Coulomb-explosion technique the complication of a mixed sample is that both the Ak^+ and Ak'^+ fragment ions contain contributions from Coulomb explosion of the homonuclear dimers as well as the heteronuclear dimer. The fragment ions originating from the homonuclear dimers and from the heteronuclear dimer will, in most cases, have overlapping kinetic-energy distributions, and as a result, the one-to-one correspondence between E_{kin} and R is lost. Thus, the directly measured kinetic-energy distribution may no longer be useful for identifying the quantum states of the dimer or for retrieving $P(R)$.

This paper demonstrates that it is possible to extract the kinetic-energy distribution $P(E_{kin})$ of the fragment ions of any specific dimer in the unavoidably mixed sample of hetero- and homonuclear dimers by using coincidence filtering. Therefore, it becomes possible to determine $P(R)$ for any one of these dimers, including the heterodimers, in this work, ^{7}Li^{39}K and ^{23}Na^{39}K.

II. EXPERIMENTAL SETUP

Figure 2 shows a schematic of the experimental setup. A detailed account was already given in Ref. [21]. A continuous beam of helium droplets is produced by expanding helium gas at a stagnation pressure of 50 bars and at a nozzle temperature of 16 K into vacuum. The average radius of the droplets is ~5 nm, corresponding to ~10^4 He atoms in each droplet [8]. The droplet beam passes through two successive pickup cells. The first (second) contains a gas of Ak (Ak′) atoms. The vapor pressure in the cells is adjusted such that some of the droplets pick up two alkali-metal atoms, resulting in the formation of either an Ak_2, Ak_2', or AkAk′ dimer. Afterwards, the doped helium droplet beam enters a velocity-map-imaging (VMI) spectrometer consisting of 3 electrodes; repeller (R), extractor (E), and ground (G). The droplet beam is crossed by a single, focused laser beam in between the repeller and extractor electrodes. The laser beam contains linearly polarized pulses with a duration of 50 fs (FWHM), a central wavelength of 800 nm, and an intensity of 1.3×10^{14} W/cm^2. The pulses are used to doubly ionize the alkali-metal dimers and thereby induce Coulomb explosion. The Ak^+ and Ak'^+ fragment ions are projected onto a position-sensitive detector backed by a TPX3CAM detector [28–30] synchronized to the 1-kHz repetition rate of the laser pulses. The TPX3CAM allows us to determine the two-dimensional velocity and the time of flight (TOF) of each ion hit. Due to the high time resolution (better than 2 ns) of the TPX3CAM, the time-of-flight measurements enable the simultaneous recording of the two-dimensional (2D) velocity images of both the Ak^+ and Ak'^+ ions [31,32]. This is crucial for the implementation of the coincident filtering of the fragment ions. The 2D velocity images constitute the basic experimental observables.

III. RESULTS AND DISCUSSION

A. Doping with Li and K atoms

1. Ion images, covariance maps, and kinetic-energy distributions from the mixed sample

In the first set of measurements, the first (second) doping cell contained Li (K) vapor, as indicated in Fig. 2(a). Figure 2(b) shows the mass-to-charge, m/q, spectrum obtained from the TOF recorded by the TPX3CAM detector. The Li (K) sample contains both ^{7}Li and ^{6}Li (^{39}K and ^{41}K). An ion hit on the detector leads to a cluster of pixels being triggered in the TPX3CAM, and for each pixel event, the x, y, TOF, and time-over-threshold (TOT) coordinates are recorded, with TOT being proportional to the intensity of light hitting the pixel. Each pixel event is time walk corrected to improve its time resolution [33]. The pixel events are divided into clusters corresponding to ion hits using a custom implementation of the DBSCAN (density-based spatial
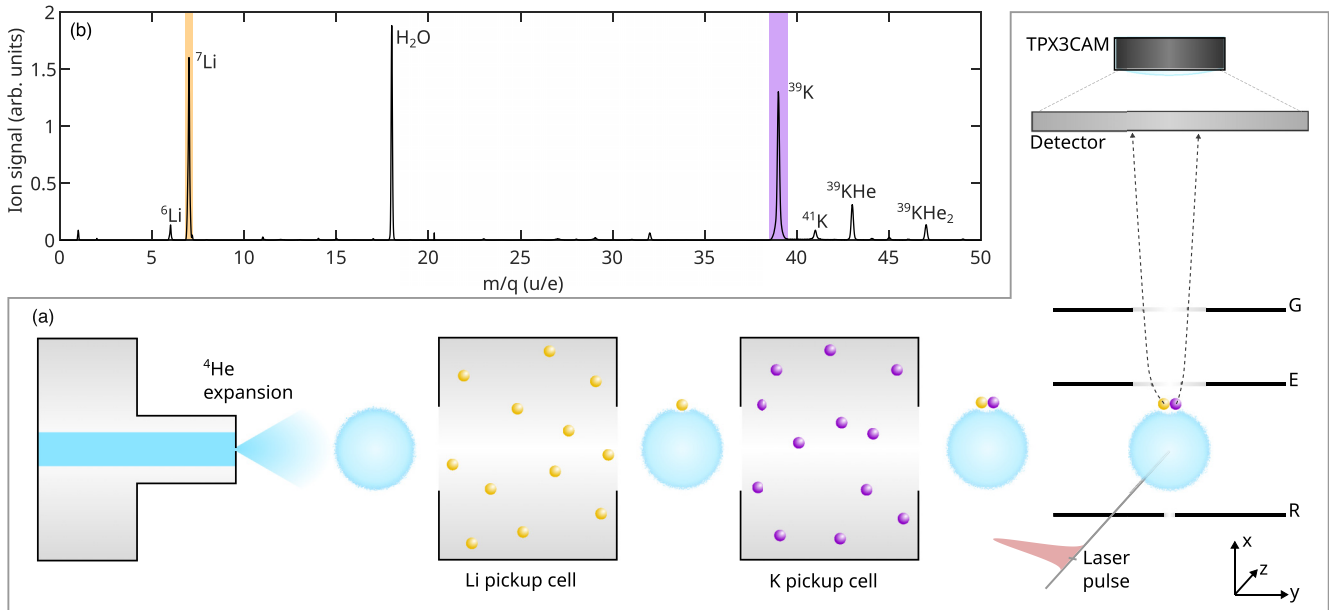
FIG. 2. (a) Schematic of the doping process and following probing process in the experiment (see the text). Not to scale. (b) Mass-to-charge spectrum obtained when the laser pulse irradiates droplets that passed through the two pickup cells containing gases of Li and K atoms.

clustering of applications with noise) algorithm [34], and the average x, y, and TOF coordinates are calculated for each cluster. Finally, the TOF of each cluster is time walk corrected again to further improve the time resolution [33]. The result is a list of ion hits, recording the two components of the projected velocity, the time of flight and the corresponding laser-shot number for each. The mass-to-charge spectrum is then calculated for each hit and binned in a histogram to give the spectrum seen in Fig. 2(b). The two peaks of interest are the ones with $m/q = 7 \, \mathrm{u}/e$ and $m/q = 39 \, \mathrm{u}/e$, assigned as the $^7\mathrm{Li}^+$ and $^{39}\mathrm{K}^+$ ions, respectively [35]. The peak at $m/q = 18 \, \mathrm{u}/e$ comes from $\mathrm{H_2O}^+$ ions created by multiphoton ionization of residual water molecules in the target chamber housing the VMI spectrometer.

The 2D velocity image of $^7\mathrm{Li}^+$ ions, displayed in Fig. 3(a1), exhibits a pronounced signal in the central region and in the outer region. The radial-velocity distribution in the detector plane $P(v_r)$, obtained by angular integration of the image, shows that the outer region consists of two overlapping peaks centered at $v_r = 6.8 \, \mathrm{km/s}$ and at $v_r = 8.1 \, \mathrm{km/s}$ [see Fig. 3(a2)]. Similarly, two peaks appear in the kinetic-energy distribution $P(E_{\mathrm{kin}})$ of the $^7\mathrm{Li}^+$ ions [Fig. 3(a3)], obtained by first Abel inverting the 2D image using the POP (polar onion peeling) algorithm [36] and then applying a Jacobian transformation to the resulting velocity distribution [20]. The central positions of the peaks are 1.69 and 2.38 eV. The lower value matches the kinetic energy a Li^+ ion acquires upon Coulomb explosion of $^7\mathrm{Li}_2$ in the $1 \, ^3\Sigma_u^+$ state, as established by recent studies on Li_2 samples [20,37].

To confirm this interpretation, we determined the covariance map of the radial-velocity distribution [38], denoted as $\mathrm{cov}(v_{r,1}, v_{r,2})$ and displayed in Fig. 3(a4). The symmetric, elongated signal that peaks at $(6.8 \, \mathrm{km/s}, 6.8 \, \mathrm{km/s})$ shows that $^7\mathrm{Li}^+$ ions with this speed or, equivalently, with E_{kin} around 1.69 eV are correlated with another $^7\mathrm{Li}^+$ ion having the same

speed or kinetic energy. Only double ionization of $^7\mathrm{Li}_2$ and subsequent Coulomb explosion of $^7\mathrm{Li}_2^{2+}$ can create such a pair of correlated $^7\mathrm{Li}^+$ ions. For completeness, we also determined the angular covariance map [39–42] of these $^7\mathrm{Li}^+$ ions, using the angular probability distribution in the detector plane for ions with v_r between 5.3 and 7.6 km/s. The result, displayed in Fig. 3(a5), exhibits two distinct diagonal lines centered at $\theta_2 = \theta_1 \pm 180°$, where θ_i, $i = 1, 2$, is the angle between an ion hit and the vertical center line [Fig. 3(a1)]. These lines demonstrate a correlation between two $^7\mathrm{Li}^+$ ions recoiling with a relative angle of 180°. Again, such a correlation confirms that the ions originate from Coulomb explosion. Finally, we note that the signal in the central area of the image comes from sources other than Coulomb explosion. This includes dissociative ionization of dimers, leading to $^7\mathrm{Li}^+$ ions with energies determined by the given dissociative potential reached and ionization of alkali-metal atoms on the droplets doped with just one atom. Isolated $^7\mathrm{Li}$ atoms that effuse into the VMI spectrometer will also be ionized, resulting in a thin line of ion signal along the v_y direction. This signal is rather intense, and it has been removed from the image, shown by the elongated rectangle, to ensure that the outermost, more interesting regions of the image are clearly visible.

The results for the $^{39}\mathrm{K}^+$ ions, displayed in Figs. 3(b1)–3(b5), are similar to the $^7\mathrm{Li}^+$ results. In the 2D velocity image [Fig. 3(b1)], there is a strong signal in the central region, again ascribed to atomic ionization and dissociative ionization, and then there are two main channels at larger radii. These channels are more separated than in the $^7\mathrm{Li}^+$ case, which can also be seen for $P(v_r)$, for which two distinct peaks, centered at $v_r = 1.4 \, \mathrm{km/s}$ and $v_r = 2.5 \, \mathrm{km/s}$, stand out [Fig. 3(b2)], and for $P(E_{\mathrm{kin}})$, with one peak at 0.42 eV and another at 1.23 eV [Fig. 3(b3)]. The latter kinetic energy matches that of $^{39}\mathrm{K}^+$ ions from Coulomb explosion of $^{39}\mathrm{K}_2$ in the $1 \, ^3\Sigma_u^+$ state. Like in the $^7\mathrm{Li}^+$ case, the symmetrically positioned island in the
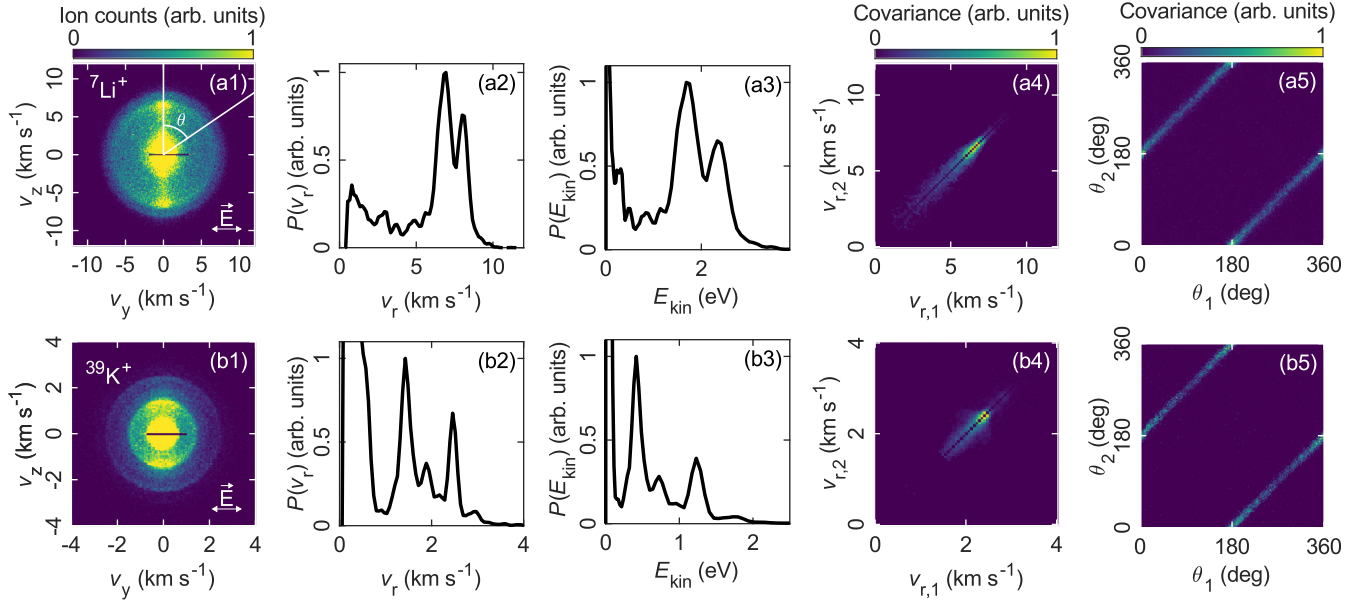
FIG. 3. (a1)–(a5) ^{7}Li^{+} results and (b1)–(b5) ^{39}K^{+} results. (a1) and (b1) Two-dimensional velocity images. (a2) and (b2) Radial-velocity distributions $P(v_r)$. (a3) and (b3) Kinetic-energy distributions $P(E_{kin})$. (a4) and (b4) Covariance maps of $P(v_r)$. (a5) Covariance map of the angular distribution for ^{7}Li^{+} ions with $5.3 \leqslant v_r \leqslant 7.6$ km/s. (b5) The same as (a5), but for ^{39}K^{+} ions with $2.2 \leqslant v_r \leqslant 2.8$ km/s.

covariance map of the radial-velocity distribution at (2.5 km/s, 2.5 km/s) [Fig. 3(b4)] confirms Coulomb explosion of ^{39}K$_2$ $1\,^{3}\Sigma_u^+$ dimers as the origin of these ions, and so do the diagonal stripes in the corresponding angular covariance map [Fig. 3(b5)].

Now we discuss the origin of the peak at $E_{kin} = 2.38$ eV in $P(E_{kin})$ for ^{7}Li^{+} and the peak at $E_{kin} = 0.42$ eV in $P(E_{kin})$ for ^{39}K^{+}. The equilibrium internuclear distance of ^{7}Li^{39}K in the $1\,^{3}\Sigma^+$ state is 4.97 Å [43]. If this heteronuclear dimer is doubly ionized, the resulting $(^{7}$Li^{39}K$)^{2+}$ dication is created with a potential energy of 2.90 eV in the Coulomb-potential approximation, compared to a ^{7}Li^{+}, ^{39}K^{+} ion pair at infinite distance. Upon Coulomb explosion, the ^{7}Li^{+} ion ends with $E_{kin} = 2.46$ eV, and the ^{39}K^{+} ion ends with $E_{kin} = 0.44$ eV due to conservation of momentum. These two values are very close to the center values of the two above-mentioned peaks in $P(E_{kin})$ for ^{7}Li^{+} and ^{39}K^{+}, respectively. Thus, we interpret the 2.38 eV peak in $P(E_{kin})$ for ^{7}Li^{+} and the 0.42 eV peak in $P(E_{kin})$ for ^{39}K^{+} as originating from laser-induced Coulomb explosion of ^{7}Li^{39}K in the $1\,^{3}\Sigma^+$ state into a $(^{7}$Li^{+}, ^{39}K^{+}) pair.

To corroborate this interpretation, we determine the co-variance map of the radial-velocity distribution for the ^{7}Li^{+} and ^{39}K^{+} ions [see Fig. 4(a)]. The strong covariance signal centered at (8.1 km/s, 1.4 km/s) shows that a ^{7}Li^{+} ion with v_r around 8.1 km/s is correlated with a ^{39}K^{+} ion with v_r around 1.4 km/s. This can also be stated as when a ^{7}Li^{+} ion with $E_{kin} = 2.38$ eV is detected, a ^{39}K^{+} ion with $E_{kin} = 0.42$ eV will also likely be detected. The only way to produce such a correlated $(^{7}$Li^{+}, ^{39}K^{+}) ion pair is through double ionization of ^{7}Li^{39}K in the $1\,^{3}\Sigma^+$ state and subsequent Coulomb explosion of the $(^{7}$Li^{39}K$)^{2+}$ dication. As for the homonuclear dimers, we determined the covariance map between the angular distribution of the ^{7}Li^{+} ions pertaining to the 2.38 eV peak and the ^{39}K^{+} ions in the 0.42 eV peak. The covariance map,

displayed in Fig. 4(b), shows correlation at a relative emission angle of 180°, as expected for Coulomb explosion of ^{7}Li^{39}K.

2. Coincident filtering: Separation of fragment ions from homonuclear and heteronuclear dimers

So far, we have shown that laser-induced Coulomb explosion leads to (partially) overlapping channels in $P(E_{kin})$ from the hetero- and homodimers present in the mixed sample. Now we discuss how coincident filtering allows the complete separation of the ^{7}Li^{+} (^{39}K^{+}) fragment ions that originate from the homodimer ^{7}Li$_2$ (^{39}K$_2$), the heterodimer ^{7}Li^{39}K, or any of the other dimer combinations of the isotopes present in the sample, ^{7}Li^{6}Li and ^{7}Li^{41}K (^{39}K^{41}K and ^{6}Li^{39}K). The filter relies on the exact division of momentum among the two fragment ions in the Coulomb explosion of a dimer. Thus, the filter for ^{7}Li$_2$ (^{39}K$_2$) works by determining those ^{7}Li^{+} ions that, within the same laser shot, are detected along with another
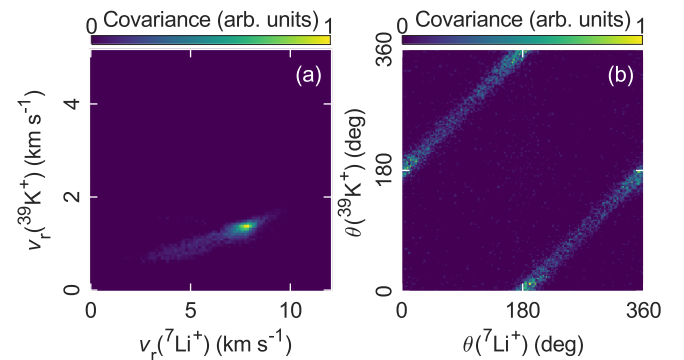

FIG. 4. (a) Covariance map of the radial-velocity distribution between the ^{7}Li^{+} ions and the ^{39}K^{+} ions. (b) Covariance map of the angular distribution between the ^{7}Li^{+} ions with $7.5 \leqslant v_r \leqslant 9.6$ km/s and the ^{39}K^{+} ions with $1.0 \leqslant v_r \leqslant 1.8$ km/s.
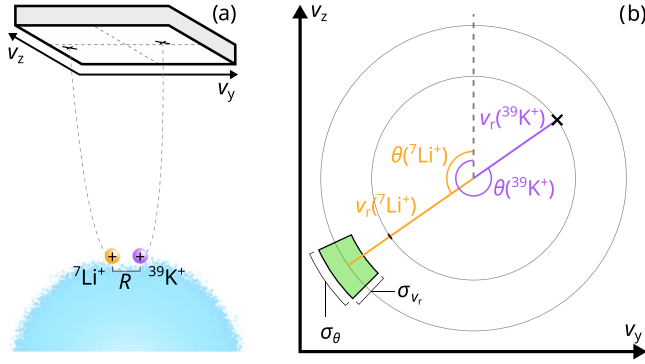
FIG. 5. (a) Illustration of the detection of the 2D velocity (v_y, v_z) of the $^7\text{Li}^+$ and $^{39}\text{K}^+$ fragment ions from Coulomb explosion of $^7\text{Li}^{39}\text{K}$. (b) Illustration of the principle of the coincidence filter for the $^7\text{Li}^{39}\text{K}$ dimer. Here σ_{v_r} and σ_θ define the velocity and angular tolerance of the filter. The values used are given in Eqs. (5) and (6).

$^7\text{Li}^+$ ($^{39}\text{K}^+$) ion having the diametrical momentum vector. Such ions can only be produced by Coulomb explosion of $^7\text{Li}_2$ ($^{39}\text{K}_2$); i.e., the filter discards $^7\text{Li}^+$ ($^{39}\text{K}^+$) produced from the Coulomb explosion of other possible oligomer combinations of the sample, such as the $^6\text{Li}\,^7\text{Li}$ ($^{39}\text{K}\,^{41}\text{K}$) dimer; any isotope combination of the LiK dimer; any isotope combination of the Li$_3$ (K$_3$), Li$_2$K, and LiK$_2$ trimers [44]; and the dissociative ionization of these oligomers. Likewise, the filter for $^7\text{Li}^{39}\text{K}$ acts by determining the $^7\text{Li}^+$ ($^{39}\text{K}^+$) ions that, within the same laser shot, are detected along with a $^{39}\text{K}^+$ ($^7\text{Li}^+$) ion with opposite momentum.

In practice, the filter is implemented in a polar coordinate system covering the detector plane (see Fig. 5). Two $^7\text{Li}^+$ ions are considered coincident if both of the following conditions are fulfilled:

$$-15^\circ < |\,\theta_1(^7\text{Li}^+) - \theta_2(^7\text{Li}^+)\,| - 180^\circ < 15^\circ,$$
$$|v_{r,1}(^7\text{Li}^+) - v_{r,2}(^7\text{Li}^+)| < 1.3 \text{ km/s}, \quad (3)$$

where subscripts 1 and 2 refer to two different $^7\text{Li}^+$ ions. Equation (3) defines the filter for identifying a $^7\text{Li}_2$ homonuclear dimer. The tolerances of the filter are chosen to encompass the full covariance lines seen in Figs. 3(a4) and 3(a5). Similarly, the filter for identifying a $^{39}\text{K}_2$ homonuclear dimer is defined by

$$-15^\circ < |\,\theta_1(^{39}\text{K}^+) - \theta_2(^{39}\text{K}^+)\,| - 180^\circ < 15^\circ,$$
$$|v_{r,1}(^{39}\text{K}^+) - v_{r,2}(^{39}\text{K}^+)| < 0.6 \text{ km/s}, \quad (4)$$

and the filter for identifying the $^7\text{Li}^{39}\text{K}$ heteronuclear dimer is defined by

$$-20^\circ < |\,\theta(^{39}\text{K}^+) - \theta(^7\text{Li}^+)\,| - 180^\circ < 20^\circ,$$
$$\left|\frac{m(^{39}\text{K})}{m(^7\text{Li})} v_r(^{39}\text{K}^+) - v_r(^7\text{Li}^+)\right| < 1.3 \text{ km/s} \quad (5)$$

when detecting $^7\text{Li}^+$ ions and

$$-20^\circ < |\,\theta(^{39}\text{K}^+) - \theta(^7\text{Li}^+)\,| - 180^\circ < 20^\circ,$$
$$\left|v_r(^{39}\text{K}^+) - \frac{m(^7\text{Li})}{m(^{39}\text{K})} v_r(^7\text{Li}^+)\right| < 0.6 \text{ km/s} \quad (6)$$

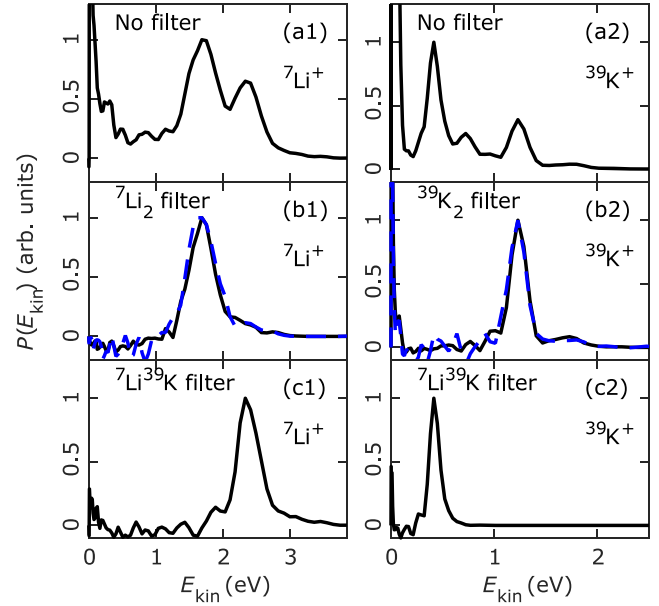

FIG. 6. Kinetic-energy distributions (black solid lines) of (a1)–(c1) $^7\text{Li}^+$ ions and (a2)–(c2) $^{39}\text{K}^+$ ions determined from those ions that passed the coincidence filter indicated at the top of each panel. Blue dashed lines show the kinetic-energy distributions of $^7\text{Li}^+$ ions in (b1) and of $^{39}\text{K}^+$ ions in (b2) obtained from droplets doped only with Li or K.

when detecting $^7\text{K}^+$ ions. Here $m(^{39}\text{K}) = 39\,\text{u}$ and $m(^7\text{Li}) = 7\,\text{u}$. The mass ratios are needed, as the even momentum sharing results in two ions with different speeds.

Now we apply the $^7\text{Li}_2$ coincidence filter, Eq. (3), to the $^7\text{Li}^+$ ions detected and determine $P(E_{\text{kin}})$ from those ions that passed the filter. The result is shown by the black solid curve in Fig. 6(b1). As a reference, we plot $P(E_{\text{kin}})$ for $^7\text{Li}^+$ ions (blue dashed curve), recorded with an empty potassium pickup cell; i.e., the helium droplets picked up only Li atoms, and thus, the only dimers formed were the Li$_2$ isotopologues. The $^7\text{Li}_2$ coincidence filter was also used for this reference measurement. The good agreement between the two curves demonstrates the desired effect of the filter to select the fragment ions corresponding to a particular dimer species, in this case $^7\text{Li}_2$, from the mixed sample. Note that $P(E_{\text{kin}})$ obtained via the coincidence filter exhibits only a single peak corresponding to dimers in the $1\,^3\Sigma_u^+$ state; i.e., there is no evidence of dimers formed in the $1\,^1\Sigma_g^+$ state, an observation consistent with previous experiments on samples of pure Li$_2$ dimers [19–21].

In a similar manner, we apply the $^{39}\text{K}_2$ coincidence filter, Eq. (4), to the $^{39}\text{K}^+$ ions detected and determine $P(E_{\text{kin}})$ from the ions that passed this filter. The result is shown by the black solid curve in Fig. 6(b2). Again, we include a reference result (blue dashed curve) depicting $P(E_{\text{kin}})$ for $^{39}\text{K}^+$ ions originating from helium droplets doped only with potassium and using the $^{39}\text{K}_2$ coincidence filter. The good agreement between the two curves shows that we can select the $^{39}\text{K}^+$ ions pertaining to the $^{39}\text{K}_2$ dimers from the mixed sample. Note that in addition to the main peak, centered at 1.23 eV, corresponding to dimers in the $1\,^3\Sigma_u^+$ state, there is a smaller peak centered at 1.70 eV. The latter is assigned to $^{39}\text{K}_2$ dimers

in the $1\,^1\Sigma_g^+$ state. This is also consistent with previous experiments on samples of pure K_2 dimers [20,21].

Having established that the coincidence filtering method works well for retrieving $P(E_{kin})$ for Coulomb explosion of both $^7Li_2$ and $^{39}K_2$ in the mixed sample, we assume that it will also work well for retrieving the signal from the heteronuclear dimer. Thus, we apply the $^7Li\,^{39}K$ coincidence filter to both the $^7Li^+$ ions [Eq. (5)] and $^{39}K^+$ ions [Eq. (6)] and determine $P(E_{kin})$ in both cases. The results are displayed in Figs. 6(c1) and 6(c2). The curves reach their maxima at 2.38 and 0.42 eV, respectively, very close to the values 2.46 and 0.44 eV expected for fragmentation of the $(^7Li\,^{39}K)^{2+}$ dication via a Coulomb potential starting from the equilibrium distance of dimers in the $1\,^3\Sigma^+$ state. Both kinetic-energy distributions display only a single peak, corresponding to the coulomb explosion of the triplet state dimers, indicating that the formation of $^7Li\,^{39}K$ dimers in the singlet state is insignificant under our current experimental conditions. This result shows that the coincidence filter is able to uniquely extract the ions that come from the heterodimer, even from a mixed sample of hetero- and homodimers.

To test the robustness of the coincidence filter, we carried out measurements at different relative pressures in the two pickup cells. If the K (Li) vapor pressure is increased (kept constant), we observe that the $^7Li^+$ ions are more likely to be found in the peak corresponding to the $^7Li\,^{39}K$ dimer rather than in the peak corresponding to the $^7Li_2$ dimer. Likewise, if the K (Li) vapor pressure is decreased (kept constant), the amplitude of $^7Li\,^{39}K$ in the $^7Li^+$ kinetic-energy spectrum decreases relative to that of the $^7Li_2$ peak. After using the two-body filter, the shape of the $^7Li\,^{39}K$ peaks remains unchanged for both the increased and decreased K vapor pressure. Thus, the kinetic-energy distributions and the retrieved internuclear distance distributions do not change when we change the doping levels of the alkali metals. We conclude that the two-body filter extracts just the desired ions pertaining to a specific dimer species from the mixed sample, regardless of how prevalent this dimer species is.

3. Distribution of internuclear distances for $^7Li\,^{39}K$

In previous studies on Coulomb explosion of homonuclear alkali-metal dimers, the distribution of internuclear distances $P(R)$ was determined from $P(E_{kin})$ via the (R, E_{kin}) relation using either the Coulomb potential for the dications or a more accurate potential from quantum chemistry calculations. For Li_2, K_2, and Rb_2 in the $1\,^3\Sigma_u^+$ state, it was found that the center of the measured $P(R)$ was within 0.05 Å of the center of the square of the wave function $|\Psi(R)|^2$ for the vibrational ground state, whereas the FWHM of $P(R)$ was about a factor of 2 larger than that of $|\Psi(R)|^2$ [21].

In the case of $^7Li\,^{39}K$, it should be possible to determine $P(R)$ from either the $^7Li^+$ fragment ions or the $^{39}K^+$ fragment ions. In Fig. 7, the red dotted curve and the black dashed curve show $P(R)$ obtained from $P(E_{kin})$ for the $^7Li^+$ ions and $^{39}K^+$ ions, respectively. As a reference we also plot $|\Psi(R)|^2$ (blue solid curve) obtained by solving the stationary vibrational Schrödinger equation with the internuclear potential from the literature [43]. First, we note that $P_{^7Li}(R)$ and $P_{^{39}K}(R)$, where the subscript labels which ion fragment the distribution is

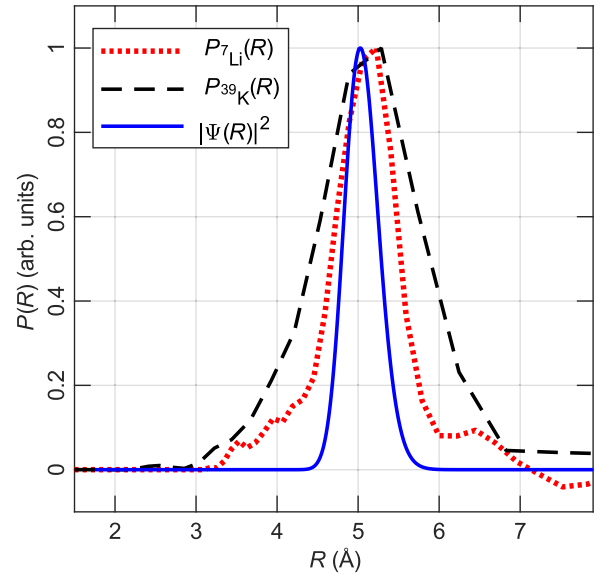FIG. 7. The distribution of internuclear distances for $^7Li\,^{39}K$ determined from the $^{39}K^+$ fragment ions (black dashed curve) and from the $^7Li^+$ fragment ions (red dotted curve). The blue solid curve shows the calculated square of the internuclear wave function for the vibrational ground state of $^7Li\,^{39}K$ in the $1\,^3\Sigma^+$ state.

obtained from, have almost the same center positions, 5.10 and 5.14 Å, i.e., values that are very close to that of the center of $|\Psi(R)|^2$, 5.04 Å. Second, we note that the FWHM of $P_{^{39}K}(R)$, 1.5 Å, is significantly larger than the FWHM of $P_{^7Li}(R)$, 0.86 Å.

If the kinetic-energy distributions measured for the two fragments, $P_{^{39}K}(E_{kin})$ and $P_{^7Li}(E_{kin})$, were solely determined by $|\Psi(R)|^2$, then $P_{^{39}K}(R)$ and $P_{^7Li}(R)$ would be identical. That is, however, not the case. As discussed in Ref. [21], the kinetic-energy distributions are broadened by various experimental factors such as the energy resolution of the VMI spectrometer and nuclear motion in the double-ionization process. Since the $^{39}K^+$ and $^7Li^+$ ions share the momentum equally in the Coulomb explosion, the $^{39}K^+$ fragment acquires only 7/46 of the total Coulomb energy, whereas the $^7Li^+$ fragment acquires a fraction of 39/46. Thus, in the transformation of the initial probability distribution $P(E_{kin})$ to the final probability distribution $P(R)$ any broadening of $P(E_{kin})$ will be amplified much more (by a factor of 39/7) for the $^{39}K^+$ case compared to the $^7Li^+$ case. This explains why $P_K(R)$ is broader than $P_{^7Li}(R)$. For comparison, the FWHM of $|\Psi(R)|^2$ is 0.50 Å; i.e., the FWHM of $P_{^7Li}(R)$ is about 70% larger than this value.

B. Doping with Na and K atoms

The different kinetic-energy distributions of $^{23}Na^+$ and $^{39}K^+$ ions from the mixed sample of the Na_2, K_2, and NaK isotopologues overlap strongly due to the similar masses of Na and K, as well as the similar structures of the dimers. Using the coincidence filter, however, the overlapping contributions can be separated, enabling the measurement of the internuclear distance distribution of the $^{23}Na\,^{39}K$ dimer. The experiment was performed by having Na vapor in the first pickup cell and K vapor in the second pickup cell.
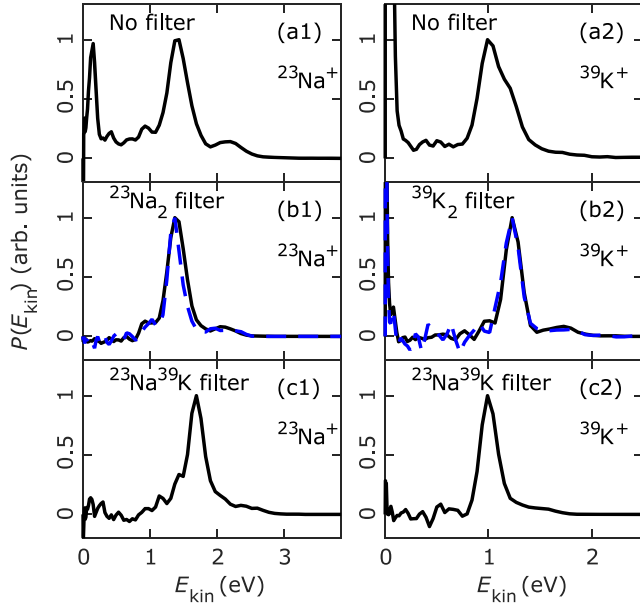
FIG. 8. Kinetic-energy distributions (black solid lines) of (a1)–(c1) $^{23}Na^+$ ions and (a2)–(c2) $^{39}K^+$ ions determined from those ions that passed the coincidence filter indicated at the top of each panel. Blue dashed lines show the kinetic-energy distribution of $^{23}Na^+$ ions in (b1) and of $^{39}K^+$ ions in (b2) obtained from droplets doped only with Na or K, respectively.

Figure 8(a1) shows $P(E_{kin})$ for the $^{23}Na^+$ ions obtained directly from the 2D image, i.e., without any coincident filtering. The 2D velocity images, radial-velocity distributions, and covariance maps, similar to those for the $^7Li\,^{39}K$ case displayed in Figs. 3 and 4, are given in the Appendix. The kinetic-energy spectrum is dominated by a large peak centered at 1.41 eV and a small peak centered at 2.13 eV. Unlike in the $^7Li\,^{39}K$ case, the major peak at 1.41 eV is not split in two. However, upon application of first the $^{23}Na_2$ filter [black solid curve in Fig. 8(b1)] and then the $^{23}Na\,^{39}K$ filter [Fig. 8(c1)], it appears that the 1.41 eV peak is, indeed, made up of two contributions. In analogy with the analysis of the $^7Li\,^{39}K$ data, the black solid curve in Fig. 8(b1) represents $P(E_{kin})$ for $^{23}Na_2$. The good agreement with the blue dashed curve showing $P(E_{kin})$ for $^{23}Na^+$ ions from droplets that picked up only Na atoms (empty K pickup cell) supports the accuracy and intended effect of the filter. The curve in Fig. 8(c1) shows $P(E_{kin})$ for $^{23}Na\,^{39}K$. This assignment is consistent with the fact that the peak position, 1.68 eV, is very close to the theoretical value, 1.65 eV, which a $^{23}Na^+$ ion acquires upon Coulomb explosion of $^{23}Na\,^{39}K$ in the $1\,^3\Sigma^+$ state. The tiny peak at $\sim$2.5 eV indicates that a small fraction of the $^{23}Na\,^{39}K$ dimers is formed in the $1\,^1\Sigma^+$ state since $^{23}Na^+$ ions from Coulomb explosion of dimers in this state will theoretically get a kinetic energy of 2.6 eV [45].

Figure 8(a2) shows $P(E_{kin})$ for the $^{39}K^+$ ions without any coincident filtering. A single broad peak is observed with an indication of a double-peak structure. Upon application of first the $^{39}K_2$ filter [black solid curve in Fig. 8(b2)] and then the $^{23}Na\,^{39}K$ filter [Fig. 8(c2)] to the $^{39}K^+$ ions, the two individual peaks are revealed. Again, we plot $P(E_{kin})$ obtained using droplets that picked up only K atoms [blue dashed
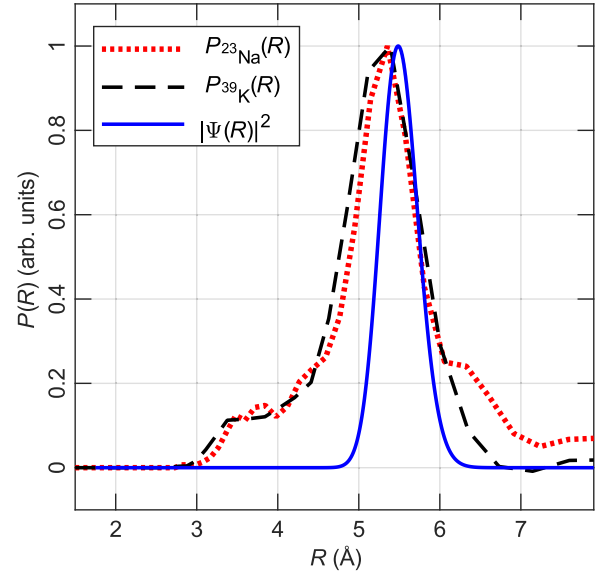

FIG. 9. The distribution of internuclear distances for $^{23}Na\,^{39}K$ determined from the $^{39}K^+$ fragment ions (black dashed curve) and from the $^{23}Na^+$ fragment ions (red dotted curve). The blue solid curve shows the calculated square of the internuclear wave function for the vibrational ground state of $^{23}Na\,^{39}K$ in the $1\,^3\Sigma^+$ state.

curve in Fig. 8(b2)]. As for the $^{23}Na^+$ ions, there is good agreement with $P(E_{kin})$ extracted from the mixed sample. The majority of the $^{39}K_2$ dimers are created in the $1\,^3\Sigma_u^+$ state (peak at 1.25 eV), although $^{39}K_2$ in the $1\,^1\Sigma_g^+$ state are also present (peak at 1.7 eV). Finally, the peak position of $P(E_{kin})$ obtained with the $^{23}Na\,^{39}K$ filter is 1.01 eV, which is close to the value expected for a $^{39}K^+$ ion created when $^{23}Na\,^{39}K$ at the equilibrium distance of the $1\,^3\Sigma^+$ state is Coulomb exploded. Overall, the data presented in Fig. 8 show that for laser-induced Coulomb explosion of the Na_2, K_2, and NaK isotopologues our coincident-filtering method is capable of extracting the individual $P(E_{kin})$ pertaining to these different dimer species, unaffected by the strongly overlapping kinetic-energy channels.

Finally, we also determine $P(R)$ of $^{23}Na\,^{39}K$ using $P(E_{kin})$ for either the $^{23}Na^+$ ions or the $^{39}K^+$ ions. Figure 9 shows $P_{^{23}Na}(R)$ (red dotted curve), $P_{^{39}K}(R)$ (black dashed curve), and, as a reference, $|\Psi(R)|^2$ for the vibrational ground state of the $1\,^3\Sigma^+$ state (blue solid curve) obtained by solving the stationary vibrational Schrödinger equation using the internuclear potential [46]. The center positions of $P_{^{23}Na}(R)$ an $P_{^{39}K}(R)$ are 5.33 and 5.28 Å, which are close to the center of $|\Psi(R)|^2$, 5.50 Å. The FWHM of $P_{^{23}Na}(R)$ is 0.92 Å, and it is 1.1 Å for $P_{^{39}K}(R)$. This similarity is expected since the smaller mass difference between ^{23}Na and ^{39}K leads to a ratio of only 39/23 for E_{kin} of the $^{23}Na^+$ and $^{39}K^+$ ions compared to an E_{kin} ratio for $^7Li^+$ and $^{39}K^+$ of 39/7 in the $^{23}Na\,^{39}K$ case. The FWHM of $|\Psi(R)|^2$ is 0.55 Å; i.e., the experimental $P(R)$ distributions are about a factor of 2 broader. This is similar to the case of the homonuclear dimers studied previously [21].

IV. CONCLUSION AND OUTLOOK

In this work, we demonstrated a method for separating the different contributions into one fragment ion species
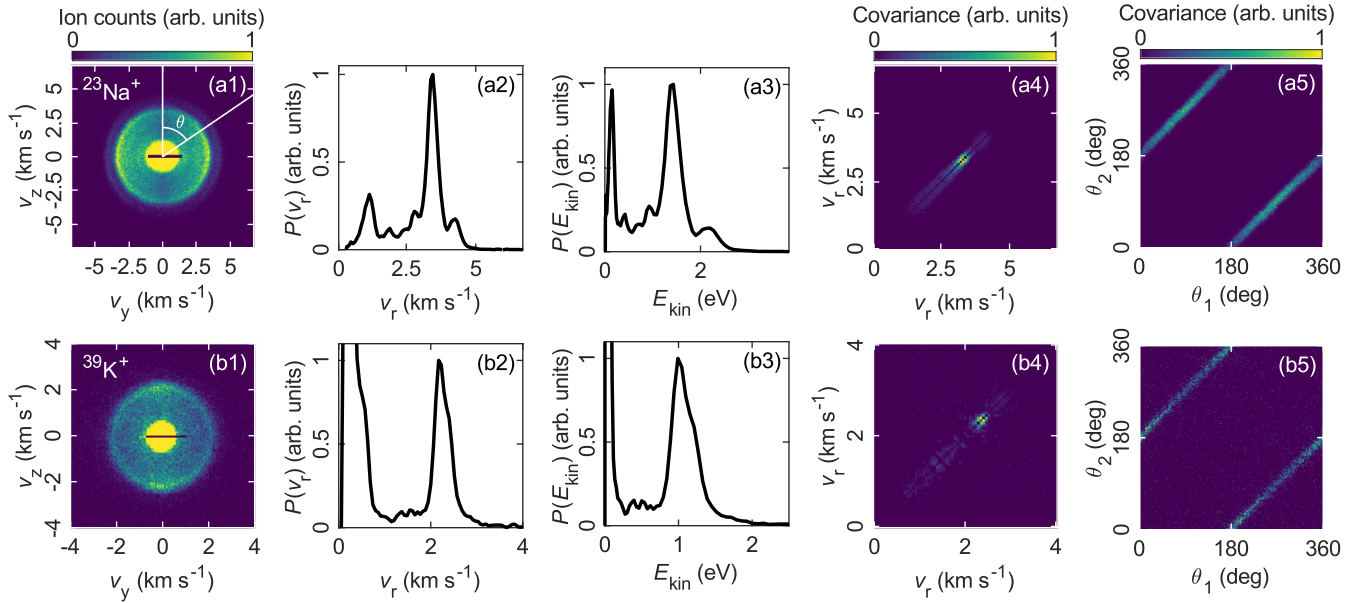
FIG. 10. (a1)–(a5) $^{23}Na^+$ results and (b1)–(b5) $^{39}K^+$ results. (a1) and (b1) Two-dimensional velocity images. (a2) and (b2) Radial-velocity distributions $P(v_r)$. (a3) and (b3) Kinetic-energy distributions $P(E_{kin})$. (a4) and (b4) Covariance maps of $P(v_r)$. (a5) Covariance map of the angular distribution for $^{23}Na^+$ ions with $2.9 \leqslant v_r \leqslant 4.0$ km/s. (b5) The same as (a5), but for $^{39}K^+$ ions with $1.1 \leqslant v_r \leqslant 3.3$ km/s.

stemming from laser-induced Coulomb explosion of different parent molecules present in a mixed sample. Our work concerned a heteronuclear alkali-metal dimer, like $^7Li\,^{39}K$, created on the surface of a helium nanodroplet in which the target sample also contained droplets doped with one of the two homonuclear alkali-metal dimers, i.e., Li_2 and K_2, as well as all of their isotopologues. We showed that the $^7Li^+$ and $^{39}K^+$ fragment ions originating from either $^7Li_2$, $^{39}K_2$, or $^7Li\,^{39}K$ can be individually filtered out using a co-incidence method based on momentum conservation in the Coulomb-explosion process. This enabled us to determine the kinetic-energy distribution of the $^7Li^+$ and $^{39}K^+$ ions from Coulomb explosion of $^7Li\,^{39}K$ and, in turn, the distribution of the internuclear distances of the initial heteronuclear dimer. To demonstrate the versatility of the coincidence filter technique, we also showed that it works as desired for $^{23}Na\,^{39}K$ in a mixed sample of the NaK, Na_2, and K_2 isotopologues.

Our method should apply generally to any mixed samples of homonuclear and heteronuclear dimers of alkali-metal atoms or alkali-metal–alkaline-earth dimers [47,48]. This also includes the separation of naturally occurring isotopologues for a dimer containing only one alkali-metal species like $^7Li\,^6Li$, $^6Li_2$, and $^7Li_2$. The technique even separates mixed-isotope, mixed-alkali-metal samples, for example, $^7Li\,^{39}K$, $^6Li\,^{39}K$, $^7Li\,^{41}K$, $^6Li\,^{41}K$, etc. Furthermore, the technique could be principally extended to mixed alkali-metal trimers and higher-order oligomers. An immediate use of the coincident-filtering technique is in time-resolved measurement of the rotational and vibrational motion of dimers (or trimers) since the different masses of the constituents lead to different nuclear dynamics. Furthermore, the filter technique should also apply to identifying droplets doped with two specific dopants inside a droplet [2,3,49,50] or with an alkali-metal atom on the surface and a molecule in the inte-

rior [32,51]. Such identification could open possibilities for exploring ion-molecule complex formation when the alkali-metal atom is selectively ionized by a femtosecond laser pulse.

The source data presented in this work and the analysis scripts used to treat them can be obtained from the authors on reasonable request. The optimized clustering and centroiding program for the TPX3CAM data is publicly available from GitHub [34].
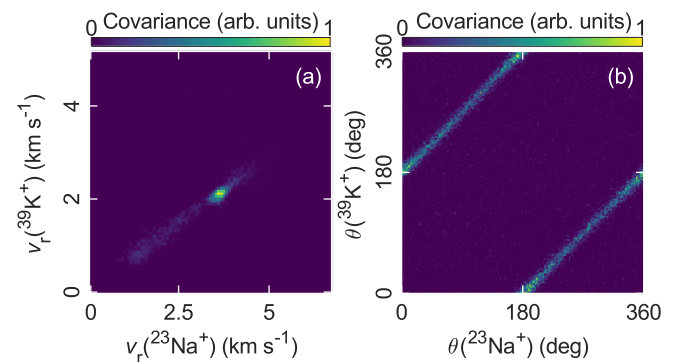
FIG. 11. (a) Covariance map of the radial-velocity distribution between the $^{23}Na^+$ ions and the $^{39}K^+$ ions. (b) Covariance map of the angular distribution between the $^{23}Na^+$ ions with $2.9 \leqslant v_r \leqslant 4.3$ km/s and the $^{39}K^+$ ions with $1.6 \leqslant v_r \leqslant 2.5$ km/s.

APPENDIX: NaK: 2D VELOCITY IMAGES, RADIAL-VELOCITY DISTRIBUTIONS, AND COVARIANCE MAPS

Figures 10 and 11 are similar to Figs. 3 and 4 but show the experimental results obtained when the helium droplets pass through the doping cells containing Na vapor in the first pickup cell and K vapor in the second pickup cell. In particular, Fig. 11 displays the radial-velocity map and the angular covariance map of the ^{23}Na$^+$ and ^{39}K$^+$ fragment ions. The clear correlation corroborates that the ions originate from Coulomb explosion of ^{23}Na^{39}K and thereby validates the filtering used to extract the results shown in Sec. III B.

[1] F. Stienkemeier and A. F. Vilesov, J. Chem. Phys. **115**, 10119 (2001).

[2] M. Y. Choi, G. E. Douberly, T. M. Falconer, W. K. Lewis, C. M. Lindsay, J. M. Merritt, P. L. Stiles, and R. E. Miller, Int. Rev. Phys. Chem. **25**, 15 (2006).

[3] S. Yang and A. M. Ellis, Chem. Soc. Rev. **42**, 472 (2013).

[4] B. Thaler, M. Meyer, P. Heim, and M. Koch, Phys. Rev. Lett. **124**, 115301 (2020).

[5] S. Albertini, E. Gruber, F. Zappa, S. Krasnokutski, F. Laimer, and P. Scheier, Mass Spectrom. Rev. **41**, 529 (2022).

[6] F. Dalfovo, Z. Phys. D **29**, 61 (1994).

[7] F. Ancilotto, G. DeToffol, and F. Toigo, Phys. Rev. B **52**, 16125 (1995).

[8] J. P. Toennies and A. F. Vilesov, Angew. Chem., Int. Ed. **43**, 2622 (2004).

[9] M. Barranco, R. Guardiola, S. Hernández, R. Mayol, J. Navarro, and M. Pi, J. Low Temp. Phys. **142**, 1 (2006).

[10] F. Stienkemeier and K. K. Lehmann, J. Phys. B **39**, R127 (2006).

[11] S. Bovino, E. Coccia, E. Bodo, D. Lopez-Durán, and F. A. Gianturco, J. Chem. Phys. **130**, 224903 (2009).

[12] G. Guillon, A. Zanchet, M. Leino, A. Viel, and R. E. Zillich, J. Phys. Chem. A **115**, 6918 (2011).

[13] F. Stienkemeier, J. Higgins, W. E. Ernst, and G. Scoles, Phys. Rev. Lett. **74**, 3592 (1995).

[14] J. Higgins, W. E. Ernst, C. Callegari, J. Reho, K. K. Lehmann, G. Scoles, and M. Gutowski, Phys. Rev. Lett. **77**, 4532 (1996).

[15] J. Higgins, C. Callegari, J. Reho, F. Stienkemeier, W. E. Ernst, K. K. Lehmann, M. Gutowski, and G. Scoles, Science **273**, 629 (1996).

[16] F. R. Brühl, R. A. Miron, and W. E. Ernst, J. Chem. Phys. **115**, 10275 (2001).

[17] J. Tiggesbäumker and F. Stienkemeier, Phys. Chem. Chem. Phys. **9**, 4748 (2007).

[18] M. Mudrich and F. Stienkemeier, Int. Rev. Phys. Chem. **33**, 301 (2014).

[19] F. Lackner, J. Poms, G. Krois, J. V. Pototschnig, and W. E. Ernst, J. Phys. Chem. A **117**, 11866 (2013).

[20] H. H. Kristensen, L. Kranabetter, C. A. Schouder, C. Stapper, J. Arlt, M. Mudrich, and H. Stapelfeldt, Phys. Rev. Lett. **128**, 093201 (2022).

[21] H. H. Kristensen, L. Kranabetter, C. A. Schouder, J. Arlt, F. Jensen, and H. Stapelfeldt, Phys. Rev. A **107**, 023104 (2023).

[22] S. Magnier, M. Aubert-Frécon, and A. R. Allouche, J. Chem. Phys. **121**, 1771 (2004).

[23] J. B. Bauer and J. P. Toennies, J. Chem. Phys. **150**, 144310 (2019).

[24] L. Kranabetter, H. H. Kristensen, A. Ghazaryan, C. A. Schouder, A. S. Chatterley, P. Janssen, F. Jensen, R. E. Zillich, M. Lemeshko, and H. Stapelfeldt, Phys. Rev. Lett. **131**, 053201 (2023).

[25] N. T. Jyde, H. H. Kristensen, L. Kranabetter, J. K. Christensen, E. Hansen, M. B. Carlsen, F. Jensen, and H. Stapelfeldt (unpublished).

[26] J. Higgins, C. Callegari, J. Reho, F. Stienkemeier, W. E. Ernst, M. Gutowski, and G. Scoles, J. Phys. Chem. A **102**, 4952 (1998).

[27] M. Mudrich, O. Bünermann, F. Stienkemeier, O. Dulieu, and M. Weidemüller, Eur. Phys. J. D **31**, 291 (2004).

[28] M. Fisher-Levine and A. Nomerotski, J. Instrum. **11**, C03016 (2016).

[29] A. Nomerotski, Nucl. Instrum. Methods Phys. Res., Sect. A **937**, 26 (2019).

[30] A. Zhao, M. van Beuzekom, B. Bouwens, D. Byelov, I. Chakaberia, C. Cheng, E. Maddox, A. Nomerotski, P. Svihra, J. Visser, V. Vrba, and T. Weinacht, Rev. Sci. Instrum. **88**, 113104 (2017).

[31] M. Fisher-Levine, R. Boll, F. Ziaee, C. Bomme, B. Erk, D. Rompotis, T. Marchenko, A. Nomerotski, and D. Rolles, J. Synchrotron Radiat. **25**, 336 (2018).

[32] S. H. Albrechtsen, C. A. Schouder, A. Viñas Muñoz, J. K. Christensen, C. Engelbrecht Petersen, M. Pi, M. Barranco, and H. Stapelfeldt, Nature (London) **623**, 319 (2023).

[33] H. Bromberger, C. Passow, D. Pennicard, R. Boll, J. Correa, L. He, M. Johny, C. C. Papadopoulou, A. Tul-Noor, J. Wiese, S. Trippel, B. Erk, and J. Küpper, J. Phys. B **55**, 144001 (2022).

[34] https://github.com/laulonskov98/pixel_centroiding_DBSCAN.

[35] ^{7}Li (^{39}K) is the most abundant isotope of Li (K) with an abundance of 95.2% (93.3%).

[36] G. M. Roberts, J. L. Nixon, J. Lecointre, E. Wrede, and J. R. R. Verlet, Rev. Sci. Instrum. **80**, 053104 (2009).

[37] In [20], ^{7}Li$^+$ ions were selectively recorded, but no selection of the parent dimer was used. The ions stem primarily from ^{7}Li$_2$ (90.54% abundance) but could also come from ^{7}Li ^{6}Li (9.23% abundance).

[38] L. Christiansen, J. H. Nielsen, L. Christensen, B. Shepperson, D. Pentlehner, and H. Stapelfeldt, Phys. Rev. A **93**, 023411 (2016).

[39] J. L. Hansen, J. H. Nielsen, C. B. Madsen, A. T. Lindhardt, M. P. Johansson, T. Skrydstrup, L. B. Madsen, and H. Stapelfeldt, J. Chem. Phys. **136**, 204310 (2012).

[40] L. J. Frasinski, J. Phys. B **49**, 152004 (2016).

[41] C. Vallance, D. Heathcote, and J. W. L. Lee, J. Phys. Chem. A **125**, 1117 (2021).

[42] C. A. Schouder, A. S. Chatterley, J. D. Pickering, and H. Stapelfeldt, Annu. Rev. Phys. Chem. **73**, 323 (2022).

[43] S. Rousseau, A. Allouche, M. Aubert-Frécon, S. Magnier, P. Kowalczyk, and W. Jastrzebski, Chem. Phys. **247**, 193 (1999).

[44] Very few trimers are actually formed because the alkali-metal vapor pressures in the pickup cells are kept low.

[45] J. Deiglmayr, M. Aymar, R. Wester, M. Weidemüller, and O. Dulieu, J. Chem. Phys. **129**, 064309 (2008).

[46] M. Aymar and O. Dulieu, Mol. Phys. **105**, 1733 (2007).

[47] F. Lackner, G. Krois, T. Buchsteiner, J. V. Pototschnig, and W. E. Ernst, Phys. Rev. Lett. **113**, 153001 (2014).

[48] F. Lackner and W. E. Ernst, J. Phys. Chem. Lett. **9**, 3561 (2018).

[49] J. D. Pickering, B. Shepperson, L. Christiansen, and H. Stapelfeldt, J. Chem. Phys. **149**, 154306 (2018).

[50] C. Schouder, A. S. Chatterley, M. Johny, F. Hübschmann, A. F. Al-Refaie, F. Calvo, J. Küpper, and H. Stapelfeldt, J. Phys. B **54**, 184001 (2021).

[51] M. Renzler, M. Daxner, L. Kranabetter, A. Kaiser, A. W. Hauser, W. E. Ernst, A. Lindinger, R. Zillich, P. Scheier, and A. M. Ellis, J. Chem. Phys. **145**, 181101 (2016).